Construction and Building Materials 335 (2022) 127487

Contents lists available at ScienceDirect

Construction and Building Materials

journal homepage: www.elsevier.com/locate/conbuildmat

Numerical simulation of the stiffness evolution with curing of pavement sections rehabilitated using cold in-place recycling technology

P. Orosa *, L. Medina, J. Fernández-Ruiz, I. Pérez, A.R. Pasandín

Universidade da Coruña, Department of Civil Engineering, E. T. S. I. Caminos, Canales y Puertos, Campus de Elviña s/n, 15071 A Coruña, Spain

ARTICLE INFO

Keywords:
3D numerical model
Cold in-place recycling (CIR)
Bitumen stabilised material (BSM)
Reclaimed asphalt pavement (RAP)
Bitumen emulsion
Triaxial testing
Nonlinear elastic behaviour
Rutting

ABSTRACT

Cold in-place recycling (CIR) technologies are becoming one of the main bets in the road sector to promote the reduction of greenhouse gas emissions. This technique also contributes to the circular economy, reusing 100% of the RAP from worn roads. In this research, numerical simulations of CIR sections are presented. The nonlinear behaviour of the CIR-base material is modelled using three predictive models based on triaxial test results. Variations in the performance depending on the type of subbase, the curing of the CIR-base material and its thickness, and the effect of the wearing-course were analysed. The response of the sections with unbound granular subbase proved to be very sensitive to variations in the parameters studied, and the increase in CIR base thickness was beneficial, while the opposite occurred with a cement-treated subbase.

1. Introduction

During the service life of any road or highway, similar to the rest of infrastructures, they are subjected to certain loads and stress levels that tend to reduce their capabilities. No matter how well designed, planned, or executed a road is, during its service life it will require periodic maintenance, and eventually, when major damage occurs, further rehabilitation is necessary to ensure an adequate level of service. When road deterioration is limited to the upper bituminous layers, an available rehabilitation technique, in line with the circular economy and the necessary respect for the environment, is cold in-place recycling (CIR) [1,2]. The advantages of this technique are already well known, there is no need to heat the mixture, it reduces the need for transportation and the usage of raw materials, thus reducing time, costs, and CO_2 emissions [3–5].

The particular feature of CIR materials is that their solid phase is mainly composed of reclaimed asphalt pavement (RAP), which does not have uniform properties [6]. This is one of the reasons why it has not been yet possible to develop a standardized procedure for the application of this technique, or standardized testing and quality control. There are numerous studies related to its mechanical properties, searching for optimal proportions of its components [7,8], studies focused on the evolution of its behaviour during curing [9,10], or related to the permanent deformations that can be expected in the long term [11,12], even construction of full-scale field trial sections to verify laboratory results [13,14]. In addition, the necessary curing period is one of the main disadvantages of cold techniques, and one of the points that require major planning and care when executing a CIR [15,16]. There is no clear consensus on the time that the CIR material layer should be allowed to cure after execution before extending a wearing layer over it or opening it to traffic flow. During curing, CIR material begins behaving as an unbound granular material (high stress-dependence [17]) and gradually acquires cohesion and stiffness until it reaches intermediate characteristics between granular material and hot mix asphalt (HMA), showing certain temperature and frequency dependence [10,18].

The nonlinear behaviour of CIR materials has been previously investigated by relatively few researchers [19–21], who have concluded that the shear strength of this type of material has a fundamental influence both on the behaviour in the short-term, before the end of curing, and in the long-term, where permanent deformations (rutting) proved to be one of the main reasons for failure in this type of mixtures [12,21]. The use of triaxial tests proved to be particularly suitable for analysing the stress-dependent behaviour of cold mixes. Monotonic triaxial tests allow obtaining the shear behaviour and failure Mohr-Coulomb envelopes, while the use of repeated load dynamic triaxial tests allows determining the resilient modulus, dependent on the applied confining pressures; and the permanent deformation response by performing a high number of load cycles tests.

* Corresponding author.
E-mail addresses: p.orosa@udc.es (P. Orosa), luis.medina@udc.es (L. Medina), jesus.fernandez.ruiz@udc.es (J. Fernández-Ruiz), iperez@udc.es (I. Pérez), arodriguezpa@udc.es (A.R. Pasandín).

https://doi.org/10.1016/j.conbuildmat.2022.127487
Received 11 February 2022; Received in revised form 29 March 2022; Accepted 10 April 2022
Available online 18 April 2022

The overall objective of all these investigations is to be able to design efficient pavements using CIR, thereby encouraging this technique to become progressively more used. In this aspect, the usual and simplest analysis to design a CIR-base is to assume elastic or viscoelastic behaviour, the way HMA layers have been traditionally designed [22]. However, the behaviour of CIR materials is more complex, and there is not enough experience in their application. CIR materials present nonlinear and stress-dependent response, and this dependency also changes with curing. Pérez et al. [23,24] considered this nonlinear behaviour and analysed different sections using bitumen-stabilised material (BSM) bases. They observed the variation of the resilient modulus with the stress level and depth, using the finite difference method (FDM), and implemented different behaviour prediction models, which were fitted from triaxial test results. They predicted principal stresses and deflections in the pavement for different thicknesses of BSM layers, taking into account the cured and uncured performance.

Following the same line, in this research, it was carried out an analysis of a pavement section after performing a CIR. For this purpose, the starting points were two typical road pavement sections widely used in the Spanish road network, which presented a reduction in their level of service, and on which cold recycling of the upper bituminous layers is applied.

2. Aims and scope

In this study, numerical simulations of pavement sections were performed to predict the performance after a road rehabilitation with a CIR, to optimize the design. The mechanical behaviour of the CIR material of the base-course, composed of 100% RAP and bituminous emulsion, was derived from previous research on its nonlinear stress-dependent response using triaxial tests [9,11]. This behaviour was then fitted through prediction models which were implemented in the commercial software FLAC3D (Fast Lagrangian Analysis of Continua in 3-Dimensions) [25].

Considering the importance of the curing period, and the lack of an adequate agreement, the simulations were performed considering different curing ages of the CIR material at ambient temperature (0 d, 3 d, 7 d, and 60 d) under partially sealed conditions. Thus, CIR material curing was considered assuming surface evaporation, and simulations were performed for scenarios with and without wearing course. Four different thicknesses were considered for the CIR-base (80, 120, 160, and 200 mm), and two different types of pre-existing subbase (cement-treated and unbound granular subbases) were analysed.

The evolution of the structural response of the sections was analysed as a function of the CIR material curing and base-course thickness. In addition, the resulting stress ratios in the CIR material were used to feed an adjusted permanent deformation model, which allowed predicting the rutting response of the sections.

3. Material characterisation

3.1. Hot-mix asphalt wearing-course (HMA)

To focus on the analysis of the nonlinear elastic behaviour of the CIR material base-course, a wearing course consisting of HMA, also called asphalt concrete (AC) according to the applied nomenclature, with a linear elastic behaviour was assumed. The parameters used were an elastic modulus $E = 5{\cdot}10^6$ kPa, and $\nu = 0.35$. It was assumed a unit weight of $\gamma = 24$ kN/m^3, and a coefficient of earth pressure at rest of value $K_0 = 0.54$. These parameters were obtained from related literature as typical values for HMA [19,23,24].

3.2. Cold in-place recycled material base-course (CIR material)

The mechanical characterization of the CIR material was obtained from experimental results of dynamic triaxial tests. These results allowed fitting the parameters of stress-dependent predictive models, published in previous contributions [9,11]. Throughout this subsection, a description of the materials used in these previous investigations, the specimen preparation, curing and testing protocols, and the fitted parameters of the respective models are summarized.

3.2.1. Reclaimed asphalt pavement and bitumen emulsion

Following the Spanish specifications for pavement recycling OC 40/2017 [26], it was proposed to study the execution of a CIR, in which the recycling of exclusively bituminous layers is conducted. Thus, the solid phase of the mixture studied in the laboratory was entirely composed of RAP.

The RAP black curve represents its size distribution containing the aged binder while the white curve represents it once the binder has been extracted. Both black and white curves, together with the gradation limits from the Spanish PG-4 [26], as well as those from TG2 and Wirtgen cold recycling manuals [2,27], are displayed in Fig. 1. While the considered RAP exceeded in one of the coarse sieves the upper limit of PG-4, it met the limits from the other two manuals, which are less restrictive with coarser size particles (Fig. 1). Thus, the RAP was considered suitable for CIR. The maximum specific gravity of the RAP, obtained according to EN 1097–6 [28] was 2425 kg/m^3, and its binder content was 4.45%, obtained by extraction following the standard EN 12697-1 [29]. The properties of the aged bitumen recovered from the RAP were a penetration grade of 32.15 dmm, and a softening point of 70.20 °C, obtained according to EN 1426 [30], and EN 1427 [31], respectively.

Following the CIR specifications [26], a bitumen emulsion labelled C60B5 REC was used. It is a cationic emulsion, with a slow curing rate, and a residual binder content of 60%, developed specifically for recycling applications. The properties of the residual binder used to prepare the emulsion were a penetration grade of 170.00 dmm, and a softening point of 36.50 °C.

3.2.2. Specimen preparation

3.2.2.1. Mixing and compaction. The CIR mixes studied in this research were prepared using a residual binder content of 2.50% and an added water content of 2.75%. These proportions were selected as the optimum in previous mechanical characterization studies with different emulsion contents [9,11], while maintaining the optimum fluid content, following the design method of the Spanish specification for cold recycling mixes [26].

An automatic mixer was used to prepare the samples, first blending the RAP with the added water for 60 s, and subsequently with the corresponding amount of bitumen emulsion for another 90 s. After mixing each sample, it was placed in 100 mm diameter moulds and compacted using a shear gyratory compactor. By EN 12697-31 [32], the parameters of the gyratory compaction were an internal rotation angle of 0.82°, 30 rpm of rotatory speed, and 600 kPa of compaction pressure. The number of compaction gyrations used was 100 ± 20, ensuring to achieve a fixed air void content of 15% for the desired height of the specimens of 100 mm.

3.2.2.2. Triaxial test specimens and curing procedure. Following the standard EN 13286-7 [33], the dimensions of the cylindrical specimens required for triaxial tests are 100 mm in diameter and 200 mm in height. These specimens were prepared by stacking two 100 mm specimens successively compacted. This preparation procedure was previously validated both by the authors and other researchers, who concluded that these specimens behaved as a single specimen when subjected to tests with stresses in the principal axis [9–11,19,21].

Once the final triaxial specimens were properly stacked, they were placed in a temperature- and humidity-controlled room to cure under environmental conditions (relative humidity of 50 ± 5% and

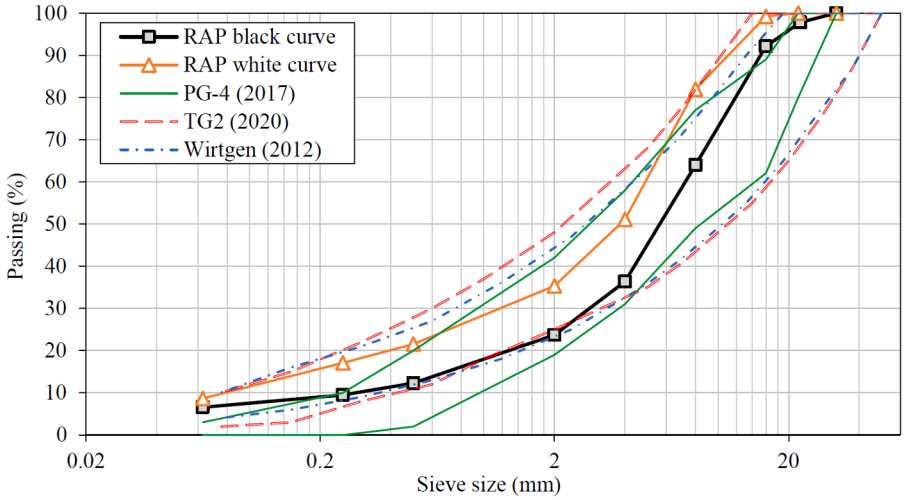

Fig. 1. RAP particle size distribution compared to the limits in cold recycling manuals.

temperature of 22 ± 2 °C). Four different curing times were considered before performing the respective triaxial tests, during which the specimens were cured under partial sealing conditions. These conditions were achieved owing to an impermeable membrane covering the lateral sides of the specimens, allowing only evaporation on the surface (Fig. 2), as occurs in real field applications. To study the short-term behaviour and evolution of the prepared CIR material, the first three curing times considered were 0 d, 3 d, and 7 d. For the curing time of 0 d, the specimens were let to cure for 4 h, to simulate their behaviour just after their placement, when the emulsion was not yet completely broken. For the curing time of 3 d and 7 d, it was considered that the emulsion was already broken, and the mixtures started to improve their mechanical properties. Finally, in addition to the very short-term performance of the mixtures, a longer curing time of 60 d was considered, for which the weight loss of the specimens and their stiffness increment were seen to stabilize [9].

3.2.3. Mechanical characteristics

3.2.3.1. Resilient moduli and nonlinear prediction models. To simulate the behaviour of the CIR material, a nonlinear elastic behaviour was assumed. The unit weight of the material was $\gamma = 22.0$ kN/m^3, the Poisson ratio, $\nu = 0.35$; and the coefficient of earth pressure at rest, $K_0 = 0.54$. To obtain the nonlinear elastic behaviour of the studied CIR material, dynamic triaxial tests were carried out at a stable ambient temperature of 22 ± 2 °C, and 1 Hz frequency, following EN 13286-7 [33], whose results were reported by Orosa et al. [9]. To conduct these tests, the equipment consisted of a hydraulic system connected to an axial-load generator (Fig. 3a), and an air compressor that applied confining pressure into a removable sealed chamber (Fig. 3b), all connected to a computer that controlled all the processes.

Fig. 2. Detail of the specimens curing under partially sealed conditions.

The results obtained allowed to adjust three prediction models of the resilient modulus (*Mr*). These models were the *k-θ* model, developed by Hicks [34], the Uzan model [35], and the NCHRP model [36], which are described, respectively, by using equations (1), (2), and (3).

$$\text{Model 1 (M1)} \quad M_r = k_1 \cdot \theta^{k_2} \tag{1}$$

$$\text{Model 2 (M2)} \quad M_r = k_1 \cdot \theta^{k_2} \cdot \sigma_d^{k_3} \tag{2}$$

$$\text{Model 3 (M3)} \quad \frac{M_r}{P_a} = k_1 \left(\frac{\theta}{P_a}\right)^{k_2} \left(\frac{\tau_{oct}}{P_a} + 1\right)^{k_3} \tag{3}$$

$$\tau_{oct} = \frac{1}{3}\sqrt{(\sigma_1 - \sigma_2)^2 + (\sigma_1 - \sigma_3)^2 + (\sigma_2 - \sigma_3)^2} = \frac{\sqrt{2}}{3}\sigma_d \tag{4}$$

where θ is known as the bulk stress ($\theta = \sigma_1 + 2\sigma_3$), σ_d is the deviator stress ($\sigma_d = \sigma_1 - \sigma_3$), τ_{oct} is the octahedral stress obtained using equation (4), and *Pa* is the atmospheric pressure (101.35 kPa) used as reference. Parameters k_1, k_2, and k_3 are material constants obtained by regression. These parameters, for each model and curing time, were obtained by Orosa et al. [9] by minimising the squared error between the experimental and predicted *Mr* results, and are listed in Table 1. It should be noted that the simulations performed with these models are considered adequate for the range of temperatures and loading frequencies in which the dynamic triaxial tests were performed.

3.2.3.2. Shear strength parameters and Mohr–Coulomb. Employing monotonic triaxial tests with different confinement pressure, the shear strength parameters cohesion (*C*) and internal friction angle (φ) were obtained by Orosa et al. [11]. Some authors already reported that these strength parameters were closely related to the permanent strain response of the material [11,12,19,23]. The same triaxial equipment shown in Fig. 3 was used, and the results for the different considered curing times are also summarized in Table 1.

With the shear parameters of Table 1, it was possible to plot the Mohr–Coulomb envelopes (Fig. 4). As expected, over the curing time, the role of the binder in the CIR mixtures becomes more significant, increasing the *C*, thanks to the bonding effect between aggregates; and reducing the φ, due to the lubricating effect caused by the binder.

3.2.3.3. Long-term cumulative permanent deformation model. The

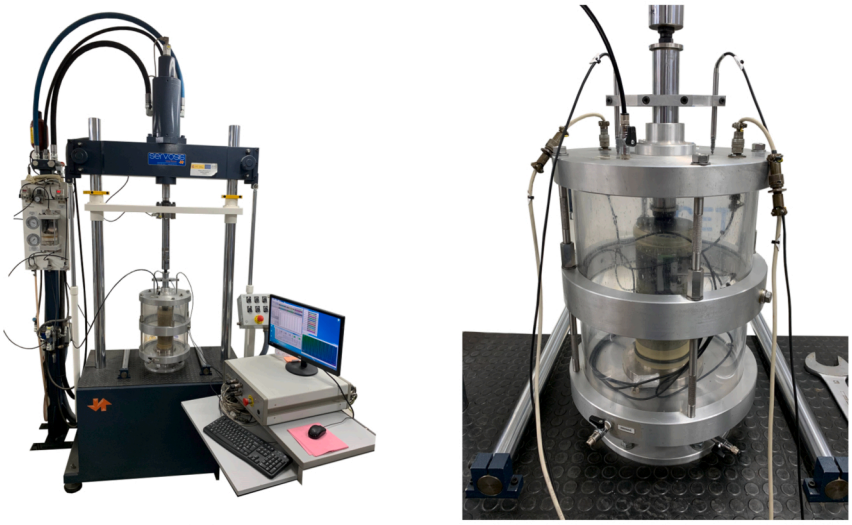

(a) (b)

Fig. 3. (a) Equipment used for triaxial tests and (b) sealed chamber detail with the strain sensors arrangement.

Table 1
Fitted parameters for the resilient modulus predictive models and shear strength parameters at the different curing ages.

Curing time	0 d			3 d			7 d			60 d		
Resilient modulus prediction models												
	k_1	k_2	k_3	k_1	k_2	k_3	k_1	k_2	k_3	k_1	k_2	k_3
M1 – Hicks	45.483	0.450		57.782	0.425		57.108	0.443		70.546	0.421	
M2 – Uzan	37.785	0.670	−0.232	43.824	0.735	−0.304	46.808	0.676	−0.231	60.133	0.611	−0.188
M3 – NCHRP	3.779	0.636	−0.607	4.222	0.704	−0.640	4.471	0.649	−0.472	4.966	0.577	−0.355
Shear strength parameters												
C (kPa)		176.93			294.77			342.94			365.27	
φ (°)		38.38			34.07			32.91			31.49	

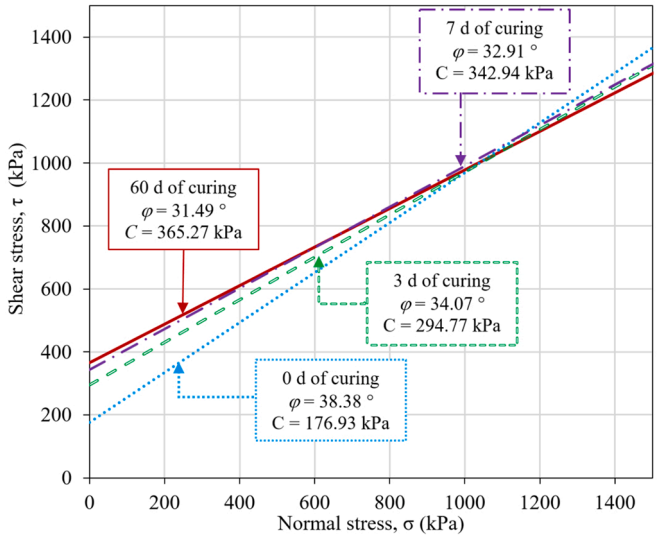

Fig. 4. Mohr–Coulomb envelopes obtained for the different curing times.

permanent deformation response in the long-term, for the cured mixture, was determined by using repeated load permanent deformation (RLPD) triaxial tests with constant confining pressure, according to the standard EN 13286-7 [33], and using the same triaxial equipment shown in Fig. 3. The experimental results were used to adjust two prediction models of the permanent deformation [11]. The most accurate model resulted to be the potential-exponential model proposed by Huurman [37] and defined in equation (5), which is a function of the number of load cycles (N) and the stress level as.

$$\varepsilon_p = A\cdot\left[\left(\frac{N}{1000}\right)^{B}\right] + C\cdot\left(e^{D\cdot\frac{N}{1000}} - 1\right) \tag{5}$$

$$A = a_1\cdot SR^{a_2};\quad B = b_1\cdot SR^{b_2};\quad C = c_1\cdot SR^{c_2};\quad D = d_1\cdot SR^{d_2}$$

where a_1, a_2, b_1, b_2, c_1, c_2, d_1, and d_2 are regression parameters fitted using the experimental results, and SR is the deviatoric stress ratio, expressed as $SR = \sigma_d/\sigma_{d,f}$, where $\sigma_{d,f}$ is the deviatoric stress at failure. The results were reported in Orosa et al. [11], and the adjusted coefficients of the permanent deformation model for the cured studied mixture are listed in Table 2. Considering the Mohr–Coulomb failure criteria, it is possible to express the SR as a function of the shear parameters, C and φ (Table 1), and the major and minor principal stresses, σ_1 and σ_3, as.

$$SR = \frac{\sigma_d}{\sigma_{d,f}} = \frac{\sigma_1 - \sigma_3}{\sigma_3\left[\tan^2\left(45^\circ + \frac{\varphi}{2}\right) - 1\right] + 2C\cdot\tan\left(45^\circ + \frac{\varphi}{2}\right)} \tag{6}$$

Authors reported that SR is a critical parameter that provides useful indications about the mechanical response to be expected from a BSM, and is closely related to its permanent deformation after a high number of loading cycles [12,21]. The same authors determined that for SR higher than 40%, it is expected that rutting takes place. The SRs were verified throughout the entire CIR-base by using equation (6), ensuring that its maximum value did not exceed the limit of 40%.

3.2.3.4. Cement-treated material subbase-course (CTM). A semi-rigid subbase of a cement-treated material (CTM) with linear elastic behaviour was assumed. When developing a new road design with this material as a subbase, it is common to use values of the modulus of

Table 2
Fitted parameters of the $\mathcal{E}_p$ prediction model.

a_1	a_2	b_1	b_2	c_1	c_2	d_1	d_2
0.022310	0.917860	0.283333	0.185589	0.010606	1.126797	2.758488	7.279381

elasticity around $6{\cdot}10^6$ kPa for its calculation [38,39]. Since here we were considering the rehabilitation with CIR of a worn-out road, we assume that the strength of the CTM has been reduced, and the considered elastic modulus was $E = 2{\cdot}10^6$ kPa. The Poisson ratio used was $\nu = 0.25$, the unit weight, $\gamma = 20$ kN/m^3, and the coefficient of earth pressure at rest of value $K_0 = 0.33$.

3.2.3.5. Unbound granular material subbase-course (UGM). A compacted unbound granular material (UGM) was considered as a flexible subbase. Although a UGM is a stress-dependent material, to simplify the model and focus on the nonlinear mechanical behavior and response of the CIR material, linear elastic behaviour with parameters $E = 3{\cdot}10^5$ kPa, and $\nu = 0.35$ was assumed for the UGM subbase-course [40,41]. It was considered a unit weight of $\gamma = 20.00$ kN/m^3, and a coefficient of earth pressure at rest of value $K_0 = 0.54$.

3.2.3.6. Subgrade. For the subgrade, it was considered the presence of a fine-graded soil with nonlinear elastic behaviour according to the model [22,42]:

$$\begin{aligned} M_r &= k_1 + k_3{\cdot}(k_2 - \sigma_d) \quad \text{when } \sigma_d \le k_2 \\ M_r &= k_1 - k_4{\cdot}(\sigma_d - k_2) \quad \text{when } \sigma_d \ge k_2 \end{aligned} \tag{7}$$

where $k_1 = 8.5{\cdot}10^4$ kPa, $k_2 = 42.8$ kPa, $k_3 = 1110$ kPa, and $k_4 = 178$ kPa are regression coefficients obtained from dynamic triaxial tests, adjusted by Thompson and Elliot [42]. For this layer it was supposed a unit weight $\gamma = 20.0$ kN/m^3, a Poisson ratio $\nu = 0.35$; and a coefficient of earth pressure at rest $K_0 = 0.54$.

The coefficients of earth pressure at rest, K_0, required to determine the in-situ stress state during the FLAC3D calculations, were obtained using the following expression (8) deduced from Hooke's law:

$$K_0 = \frac{\sigma_h}{\sigma_v} = \frac{\nu}{1-\nu} \tag{8}$$

Although the above formula (8) is only valid for linear–elastic materials, no other experimental data was available and, since this parameter does not affect the stresses and strains induced by traffic loads, the obtained values were considered to be an acceptable overall estimation for the materials analysed.

4. Pavement sections and numerical model description

The Spanish guidelines for new pavement sections design [43], as well as the experience in recent years, showed that a typical road section is composed of different thicknesses of bituminous layers on top, over flexible (unbound granular) or semi-rigid (cement-treated) bases, and different categories of subgrade. In this study, both scenarios were considered. On the one hand, a semi-rigid pavement with a cement-treated base and cracking problems in the upper bituminous layers (Fig. 5a); and on the other hand, a section with a flexible base composed of granular material (Fig. 5b) and distressed bituminous layers on top of it. In Spain, it is common to perform a CIR on medium-low traffic roads, and it is especially recommended for semi-rigid subbases [44].

Both rehabilitated pavement sections consisted of an HMA wearing-course with a thickness of 50 mm and a CIR-base with a starting thickness of 120 mm, complying with the recommendations of the Spanish OC 40/2017 [26]. These bituminous layers were executed over a pre-existing 30 mm layer of CTM (Section 1), or 40 mm layer of UGM (Section 2), and a fine-graded soil subgrade (Fig. 5). To evaluate the influence of CIR-base thickness, three additional thicknesses (80, 160, and 200 mm) were analysed. In addition, to simulate the construction moment before the execution of the HMA wearing-course, two scenarios were analysed in each case: Section 1 with and without HMA (CTM_H, and CTM_0, respectively) and Section 2 with and without HMA (UGM_H, and UGM_0, respectively). The load configuration considered for the numerical simulation was that corresponding to a single axle of 130 kN with two dual tires (65 kN on each set of tires). For this purpose, two homogeneous circular loads p = 900 kPa with radius 107.2 mm, separated a distance of 343 mm between centres, were applied (Fig. 5).

To obtain the stresses and strains in the studied section, a model was built using the software FLAC3D [25], which allows the simulation of the elastic–plastic behaviour of the materials used in the pavement using a specific finite differences calculation. Using FLAC3D, the pavement

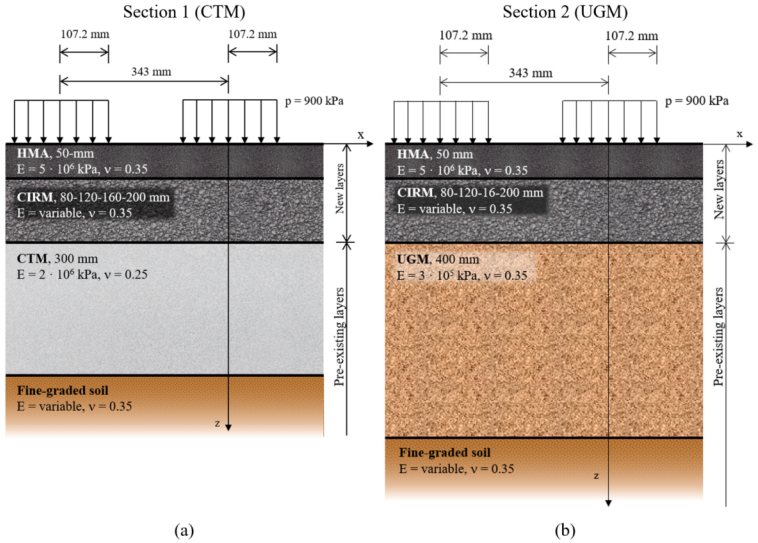

Fig. 5. Rehabilitated pavement sections after CIR used in numerical simulation: (a) Section 1 (CTM) assuming semi-rigid subbase; (b) Section 2 (UGM) assuming flexible subbase.

layers were divided into polyhedral elements that formed a 3D mesh (Fig. 6). Each of these elements behaves according to established stress–strain law, responding to the loads applied and the considered boundary conditions. Given the special symmetry characteristics of the study (both in terms of loads and geometry), it was possible to study half of the problem, by imposing the proper boundary conditions, thus reducing the computational costs. The applied boundary conditions were:

- On plane x = 0, displacements in x–direction were prevented (symmetry plane).
- On plane y = 0, displacements in y–direction were prevented (symmetry plane).
- On the lateral edge of the grid, displacements in y- and x-directions were prevented. This lateral edge of the grid was placed sufficiently far away from the load (1.40 m) so that its influence on the results was minimal.
- All movements were restricted at the bottom of the mesh, on plane z = 1.24 m.
- The groundwater level was assumed to be sufficiently deep so as not to interfere with the numerical calculations (the materials in the studied section are not underwater). Thus, the total stresses are equal to the effective stresses. Total adhesion (equality of horizontal displacements) was assumed for the contact between the layers.

5. Results and discussion

5.1. Comparison of the sections response using the three models of resilient behaviour

Three prediction models of the resilient modulus were used in FLAC3D to simulate the behaviour of the CIR material of the base. The parameters of the models were fitted from experimental results of dynamic triaxial tests (Table 1). The stress dependence of the models allowed to analyse the variation of *Mr* with depth under the considered tyre load (Fig. 5). In addition to *Mr* variations, three critical responses in the CIR-base were also tracked:

- Peak deflection obtained in the higher fibre of the CIR-base (d_B).
- Peak radial strain obtained in the lower fibre of the CIR-base (ε_{rB}).
- Peak stress ratios obtained in the entire CIR-base (*SR*).

Fig. 7 illustrates these *Mr* variations for the studied sections with HMA on top (CTM_H and UGM_H) and without HMA (CTM_0 and UGM_0), for the different curing times (0 d, 3 d, 7 d, and 60 d). Only the case of sections with CIR-base thickness of 120 mm (t120) is represented. The coloured markers represent the case of the sections with HMA, while the blank markers represent the case of the sections without HMA. The different shape of the markers represents the different prediction model used (M1, M2, and M3).

The most remarkable outcome in Fig. 7 is the significantly higher *Mr* variations in the cases without HMA, as expected. It is precisely the effect of the HMA wearing course to reduce the stresses that reach the base layer. Thus, the cases without the HMA layer suffer higher stresses, therefore exhibiting higher *Mr,* even more than twice as high as the case with HMA in the superior section of the layer (stress-dependent behaviour). In all cases, the *Mr* decreases with depth, as do the stresses. As curing time progresses (downward evolution of the graphs), *Mr* increases in all cases. Comparing the results among the three models, M2 and M3 showed the most similar results in all cases. In the cases of the section with HMA, M1 always presented the highest *Mr*, while in the cases of sections without HMA, M1 showed higher Mr in the lower fibre and lower in the upper fibre. The biggest difference between models M2 and M3 compared to M1 is in the cases of the section without HMA, which are more sensitive, presenting higher tensional variation.

Table 3 lists together the peak responses of the 120 mm-thickness CIR-base obtained using the three models, for the two studied sections with and without HMA, at the different curing times. The main differences are again observed when using M1 compared to M2 and M3. In particular, M1 always predicts the lowest deflections in the highest fibre of the CIR-base, so its predictions were slightly on the unsafe side. The results of the other two models were more similar, however since the M3 (NCHRP model) is the newest and most advanced model, it was selected to perform the rest of the analysis in this research.

Four different CIR-base thicknesses were also compared in this study. Figs. 8 and 9 show the variation of *Mr* with depth using only the selected NCHRP model (M3) for the different sections, varying the CIR-base thickness. Fig. 8 represents the cases of sections without HMA (CTM_0 and UGM_0), while Fig. 9 represents those with HMA (CTM_H and UGM_H). Since the curing of the CIR material was considered without HMA on top (partially sealed), it is important to mention that the results in Fig. 9 refer to the moment just after placement the HMA wearing-course (i.e., after allowing the CIR material to cure uncovered). Different types of lines and colours indicate different CIR-base thicknesses and curing times, respectively.

Fig. 8 shows in all cases the growth of *Mr* in the CIR-base with the curing time, both considering semi-rigid and flexible subbases. However, concerning the variation of *Mr* values with the thickness of the base, the pattern is different between the two sections. Section CTM_0 showed significant variation in the *Mr* values in the upper half of the thickness, while in the lower half it becomes more stable. However, section UGM_0 presented variation throughout the entire thickness of the base layer, also showing higher maximum *Mr* and lower minimum *Mr* compared to section CTM_0. For example, for the case of the 200-mm thickness CIR-base at 7 d, the variation between the minimum and maximum *Mr* was $1.29 \cdot 10^6$ kPa in the CTM_0 section, but $2.27 \cdot 10^6$ kPa

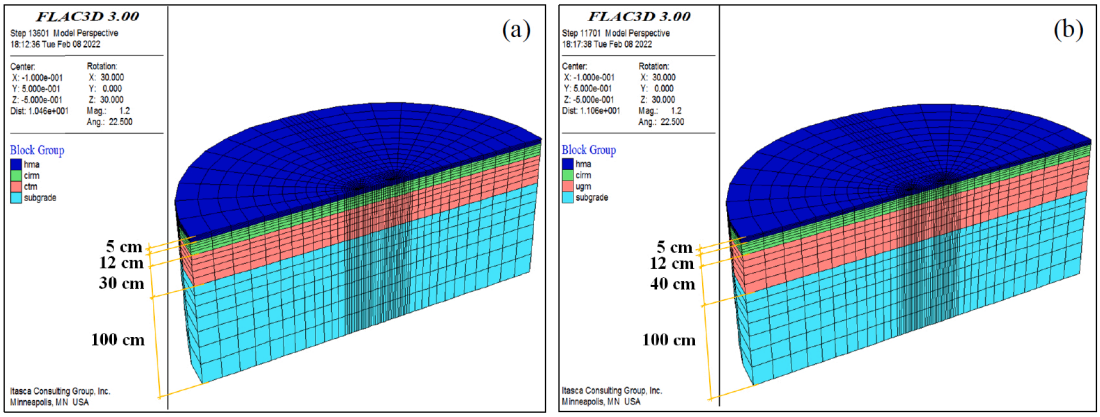

Fig. 6. Details of the mesh and coordinate system used for the 120-mm thickness CIR-base cases: (a) Section 1 (CTM); (b) Section 2 (UGM).

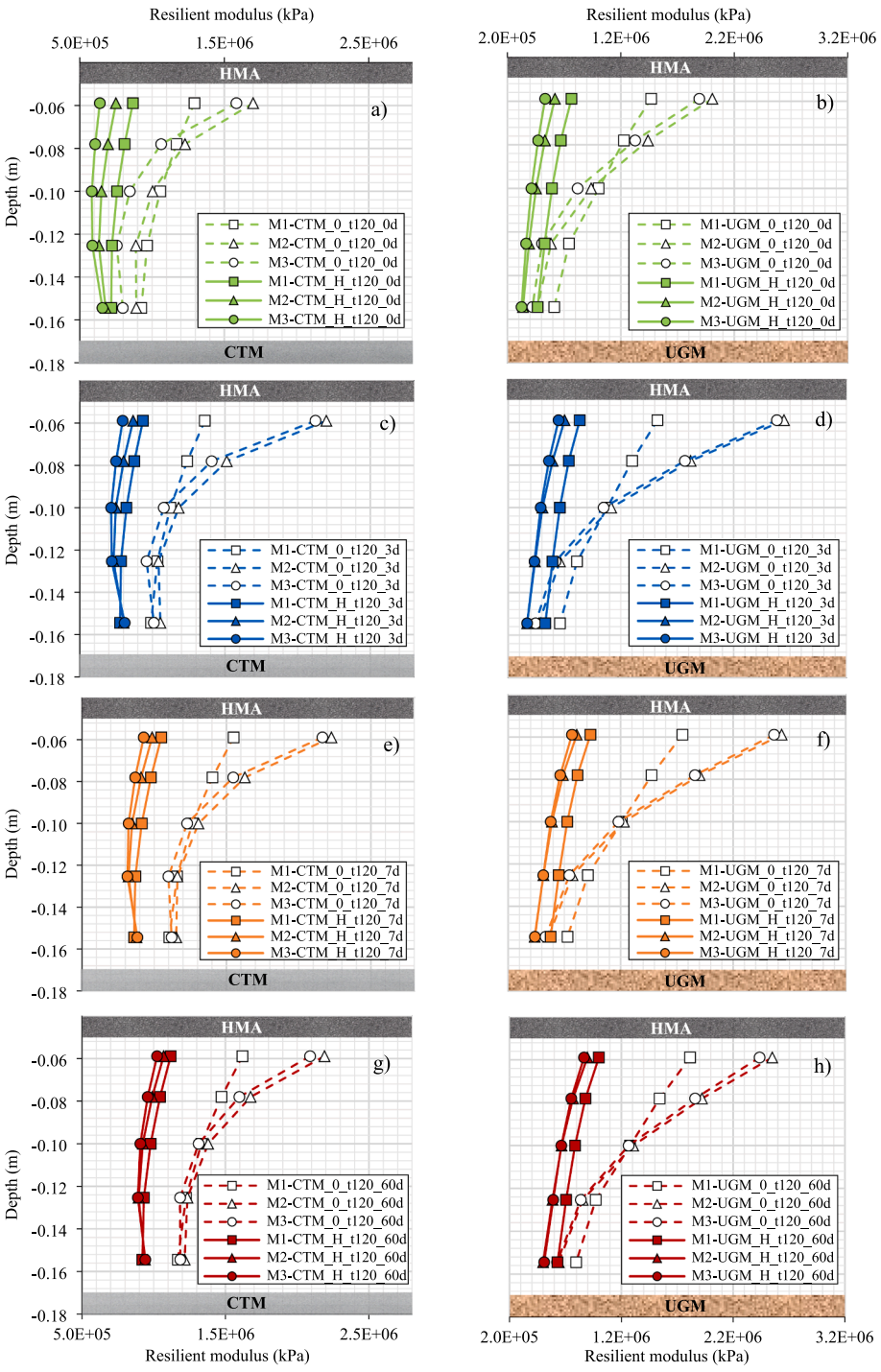

Fig. 7. Resilient modulus variations in the 120-mm thickness CIR-base for the studied sections and curing times, using the three nonlinear predictive models.

in the UGM_0 section. This higher stability shown in section CTM_0 is caused by the higher stiffness of the subbase, which helps to better resist the stresses applied in section CTM_0. However, in section UGM_0, the CIR material is the stiffer one (compared to the granular subbase material), presenting higher maximum *Mr* in the upper part, but also lower *Mr* in the lower part due to the existence of tensile stresses, compared to section CTM_0.

Fig. 9 shows the smaller variation of *Mr* in all cases, due to the smoother reduced stresses reaching the base layer owing to the HMA wearing-course. However, the section with the flexible subbase-course (UGM_H) also presents variation throughout the entire thickness, reducing the values towards the lower part of the base, while in the CTM_H section the values are more stable. Comparing again the case of the 200-mm thickness CIR-base at 7 d, the variation between the minimum and maximum *Mr* was $1.98 \cdot 10^5$ kPa in the CTM_H section, but $4.12 \cdot 10^5$ kPa in the UGM_H section. *Mr* variations are one order of magnitude more stable than the cases without HMA in both cases, but the CTM-subbase section still shows a much more stable *Mr* variation than that with UGM-subbase.

It is worth noting that in Figs. 8 and 9 the two analysed sections with semi-rigid subbase (CTM), both with and without HMA, show a general increase in *Mr* with decreasing the CIR-base thickness, for each curing time. However, the opposite occurs with flexible subbases (UGM), reducing *Mr* as the CIR-base thickness decreases. Higher *Mr* values will

Table 3
Peak predicted responses in the 120-mm thickness CIR-base for the studied sections and curing times, using the three nonlinear models (deflections in mm, strains in με, and stress ratios in %).

Curing	Model	CTM_0			CTM_H			UGM_0			UGM_H		
		d_B	ε_{rB}	SR	d_B	ε_{rB}	SR	d_B	ε_{rB}	SR	d_B	ε_{rB}	SR
0 d	M1	0.242	28.1	46.0	0.201	21.2	48.8	0.444	393.1	96.3	0.344	170.9	99.9
	M2	0.244	27.7	46.1	0.203	20.4	48.5	0.446	382.3	93.5	0.348	170.0	99.6
	M3	0.245	27.5	45.9	0.204	20.2	48.6	0.448	387.0	91.4	0.349	169.8	99.6
3 d	M1	0.240	28.7	36.3	0.199	21.9	37.8	0.438	306.3	95.9	0.341	172.0	58.6
	M2	0.241	28.3	36.7	0.201	21.1	39.4	0.439	295.7	90.4	0.346	171.5	55.2
	M3	0.241	28.1	36.7	0.202	20.8	39.0	0.440	297.3	89.8	0.347	171.5	54.2
7 d	M1	0.239	28.9	33.5	0.198	22.2	34.9	0.436	301.9	84.3	0.340	171.9	47.6
	M2	0.239	28.5	33.7	0.200	21.7	36.0	0.437	295.9	79.2	0.344	171.1	45.6
	M3	0.240	28.4	33.7	0.200	21.4	35.7	0.437	296.8	78.9	0.344	171.3	45.4
60 d	M1	0.237	29.3	33.3	0.196	22.8	34.7	0.434	301.4	77.7	0.338	172.3	43.9
	M2	0.238	29.0	33.5	0.197	22.3	35.7	0.435	295.9	75.4	0.341	171.1	43.7
	M3	0.238	28.9	33.5	0.198	22.2	35.4	0.435	297.5	75.2	0.341	171.3	43.7

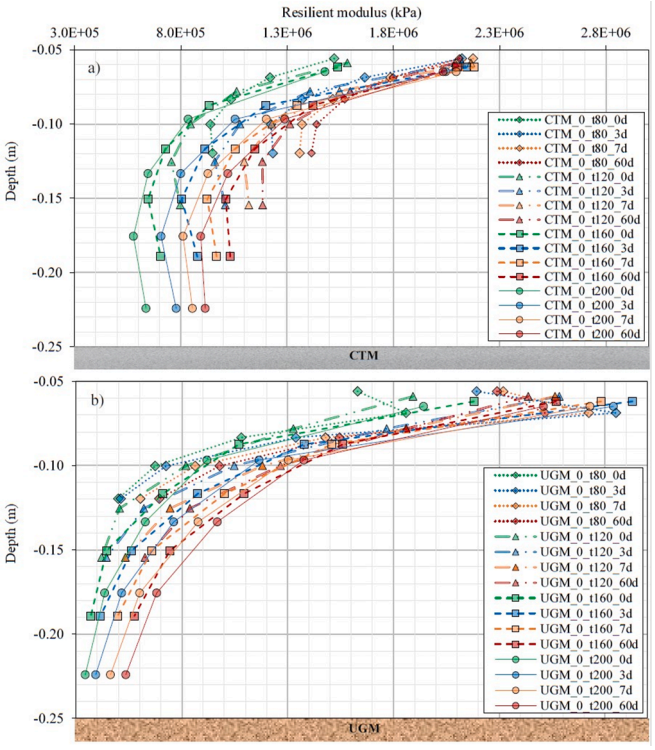

Fig. 8. Resilient modulus variations in sections without HMA, for the different CIR-base thickness and curing times, using predictive model 3: a) CTM subbase, b) UGM subbase.

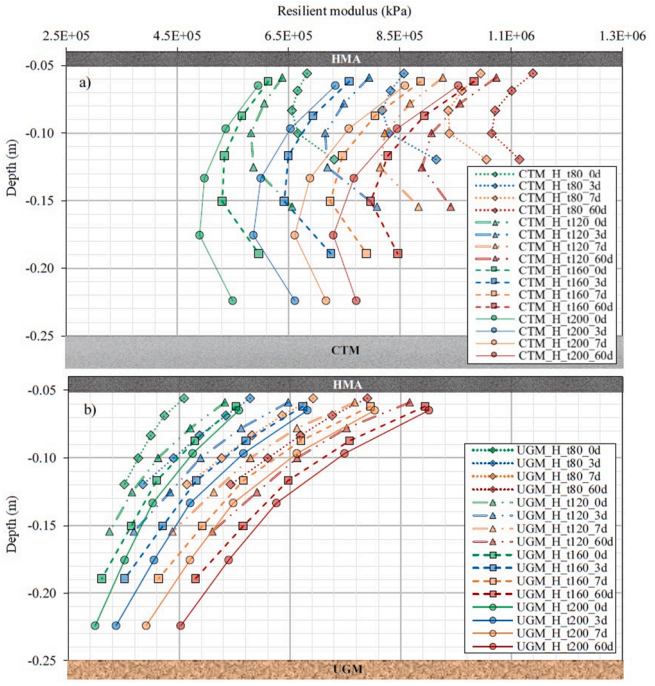

Fig. 9. Resilient modulus variations in sections with HMA, for the different CIR-base thickness and curing times, using predictive model 3: a) CTM subbase, b) UGM subbase.

lead to stronger layers, which exhibit higher failure stress levels, with lower stress ratios, and lower deflections.

5.2. Influence of curing, subbase type, and CIR-base thickness on the CIR material stress ratios

Based on the resulting principal stresses in the sections, it was possible to calculate the *SR*s in each case using the expression (6). Fig. 10 illustrates the peak *SR*s obtained in the CIR-base layer for the different curing times, depending on the base thickness considered. It is also marked in Fig. 10 in green the range corresponding to *SR*s lower than 40%. Jenkins et al. [12] recommend this *SR* limit to avoid permanent deformations in BSMs with a reliability of 80% to 90%.

Fig. 10 shows the very different trends of the *SR*s in the CIR-base when using the section with CTM or UGM subbase courses. The *SR*s in Fig. 10 were much more stable with the CTM subbase, due to its higher stiffness than those with the UGM subbase, similar to what occurred in Figs. 8 and 9 with the *Mr* variations. Another interesting difference was the trend of the peak *SR*s regarding the CIR-base thickness. Peak *SR*s in sections with the UGM subbase showed a general decrease as the CIR-base thickness increased, while the opposite occurred with the CTM subbase. The high stiffness of the CTM subbase helps to resist adequately the stresses even with the lowest CIR-base thickness. Thus, when the thickness of the CIR-base increases in the section with CTM subbase, the stresses that were previously supported by the CTM become now supported by the CIR material, and its *SR* increases slightly. However, in the case of the sections with UGM subbase, the CIR material of the base is the stiffer of the two materials and its resistant role is more important than in the other section. In this case, increased thickness is positive for the CIR-base to better distribute the applied stresses, and reduce its peak *SR*s. In Table 4 the different *SR*s obtained for the different sections (subbase type and CIR-base thickness) and curing times are listed. In the case of UGM_0 at 0 d of curing for the lower thicknesses, there is an exception to the discussed trend (Fig. 10). Due to the lower stiffness of

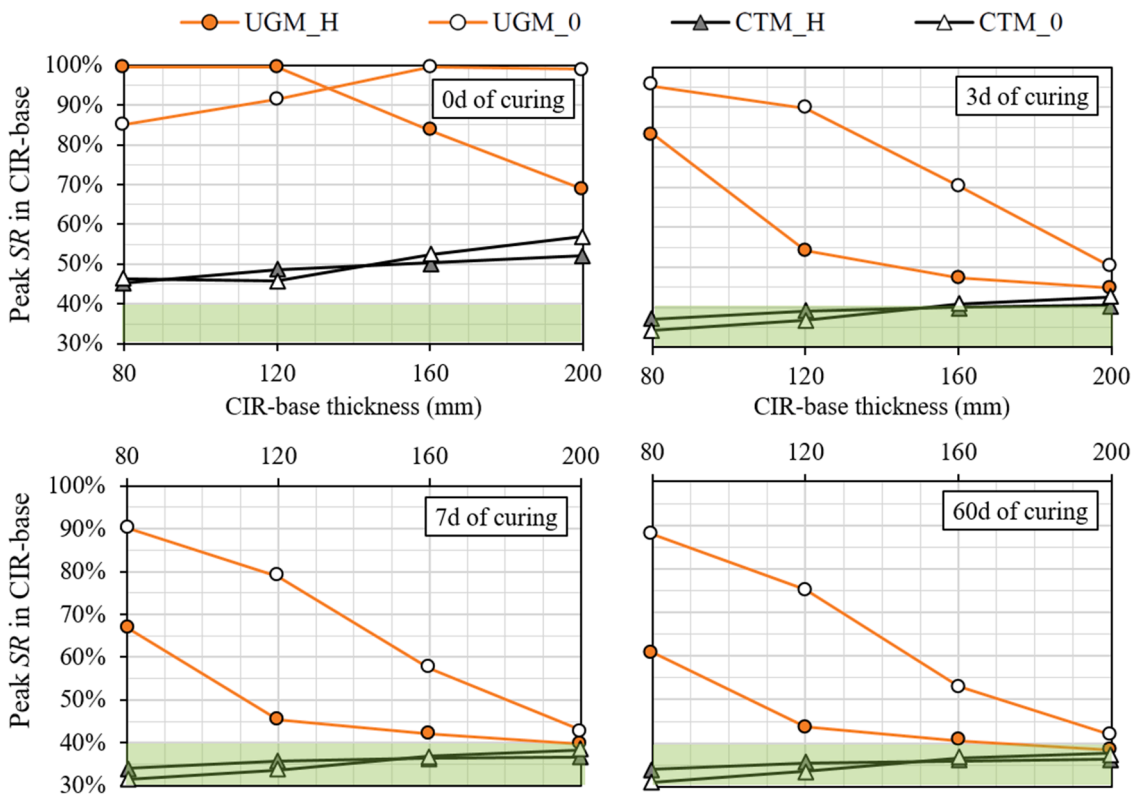

Fig. 10. Peak stress ratios variation in the CIR-base for the different thicknesses and curing times.

Table 4
Peak deflections (in mm), strains (in με), and stress ratios (in %) of the analysed sections at the different curing stages.

	CTM_0				CTM_H				UGM_0				UGM_H			
t	80	120	160	200	80	120	160	200	80	120	160	200	80	120	160	200
	0 days of curing															
d_H					0.203	0.208	0.211	0.214					0.377	0.352	0.333	0.320
d_B	0.242	0.245	0.247	0.248	0.199	0.204	0.207	0.210	0.507	0.448	0.409	0.381	0.374	0.349	0.330	0.316
d_S	0.163	0.149	0.138	0.128	0.134	0.127	0.120	0.115	0.207	0.184	0.167	0.153	0.170	0.156	0.144	0.134
ε_{rH}					127.3	137.0	140.9	143.2					177.1	161.2	154.1	149.9
ε_{rB}	18.6	27.5	27.3	24.1	24.4	20.2	16.5	13.5	503.9	387.0	235.3	164.2	230.7	169.8	137.5	112.4
ε_{rS}	267.4	237.3	215.7	196.7	217.8	202.2	187.2	174.8	370.8	321.7	286.3	257.3	302.0	269.9	243.5	222.1
SR	46.2	45.9	52.5	56.9	45.4	48.6	50.4	52.2	85.0	91.4	96.6	99.0	99.5	99.6	83.6	68.8
	3 days of curing															
d_H					0.202	0.206	0.209	0.212					0.374	0.35	0.332	0.318
d_B	0.241	0.241	0.243	0.243	0.198	0.202	0.205	0.208	0.499	0.44	0.404	0.377	0.371	0.347	0.329	0.314
d_S	0.163	0.149	0.138	0.127	0.134	0.127	0.121	0.115	0.21	0.185	0.167	0.152	0.17	0.156	0.144	0.134
ε_{rH}					122.9	132.5	136.5	139.0					171.6	156.8	149.6	145.5
ε_{rB}	18.6	28.1	27.3	24.0	25.2	20.8	16.9	13.8	422.9	297.3	214.9	161.6	225.5	171.5	136.6	112.2
ε_{rS}	267.5	236.2	214.8	195.9	217.4	201.6	187.2	174.8	375.8	323.4	286.8	257.1	302.4	269.7	243.7	222.2
SR	34.2	36.7	40.7	42.5	36.9	39.0	40.0	40.4	95.3	89.8	70.4	50.2	83.3	54.2	47.4	44.8
	7 days of curing															
d_H					0.201	0.204	0.207	0.209					0.372	0.347	0.329	0.314
d_B	0.240	0.240	0.241	0.240	0.196	0.2	0.203	0.205	0.495	0.437	0.401	0.374	0.369	0.344	0.326	0.311
d_S	0.163	0.148	0.137	0.127	0.133	0.126	0.12	0.114	0.21	0.184	0.166	0.152	0.17	0.155	0.143	0.133
ε_{rH}					120.0	129.2	133.1	135.5					167.7	152.6	145.2	141.1
ε_{rB}	18.8	28.4	27.6	24.0	26.0	21.4	17.5	14.4	397.1	296.8	214.4	160.5	226.5	171.3	136.6	112.2
ε_{rS}	266.8	235.2	213.8	194.9	216.5	200.4	185.9	173.3	375.9	322.3	285.7	255.9	301.8	269.3	242.8	220.8
SR	31.4	33.7	37.0	38.4	34.1	35.7	36.4	36.7	90.2	78.9	57.5	42.9	66.8	45.4	42.0	39.7
	60 days of curing															
d_H					0.199	0.202	0.205	0.206					0.370	0.344	0.325	0.310
d_B	0.239	0.238	0.239	0.238	0.195	0.198	0.200	0.202	0.493	0.435	0.398	0.371	0.367	0.341	0.322	0.307
d_S	0.162	0.148	0.136	0.126	0.132	0.125	0.119	0.113	0.209	0.184	0.166	0.151	0.170	0.155	0.142	0.132
ε_{rH}					117.5	126.0	129.9	132.1					163.6	148.4	141.0	137.1
ε_{rB}	19.3	28.9	28.0	24.4	26.7	22.2	18.1	15.0	393.6	297.5	214.3	160.6	227.5	171.3	136.6	112.1
ε_{rS}	266.0	234.0	212.4	193.5	215.2	198.6	184.0	171.1	374.6	320.9	284.6	254.4	300.9	267.6	241.1	219.2
SR	31.1	33.5	36.5	37.6	34.0	35.4	35.9	36.2	88.0	75.2	52.9	41.9	60.9	43.7	40.5	38.3

the CIR material at 0 days of curing (Fig. 8), and the lower thicknesses, the stresses that would produce higher *SR*s occur deeper in the section.

Concerning the evolution of *SR*s with curing, a general trend towards reduction can be observed in all cases (Table 4). Plotting the variation of *SR*s vs curing time in Fig. 11 it is simpler to observe that after 7 d the *SR*s become stable. It can be concluded that in terms of *SR*, 7 days of curing is an adequate time for the CIR material to develop satisfactory characteristics compared to what can be expected after full curing. For optimal development of the properties of the CIR material, the placement of the HMA wearing-course on the top of the CIR-base can be done after 7 d of curing, without waiting longer, as the improvement after 60 d is not expected to be significant in terms of *SR*s.

5.3. Influence of curing, subbase type, and CIR-base thickness on the section peak responses

From the conducted simulations, the deflections produced in the upper fibres of the HMA wearing-course (d_H), CIR-base (d_B), and subgrade (d_S) were also checked. Radial strains in the bottom fibres of the HMA wearing-course (ε_{rH}) and CIR-base (ε_{rB}), and vertical strain in the upper fibre of the subgrade (ε_{vS}) were obtained. All these results for the different sections (type of subbase and CIR-base thickness) and curing times are also listed in Table 4. The variations of deflections and strains with the thickness of the CIR-base layer were similar for all curing times. This trend is shown in Fig. 12 for the case at 7 d of curing. Fig. 12a shows the results of deflections in the upper fibres of HMA, CIR material, and subgrade, and Fig. 12b shows the horizontal strains in the lower fibres of HMA and CIR material.

Fig. 12 shows the greater influence of base thickness on the responses of the section with flexible subbase (UGM). While the results of the CTM section were quite stable, those of the UGM section were more sensitive, showing greater decreases in deflections and strains when increasing the CIR-base thickness. These differences in the results are caused by the same reason as the variability in the *SR*s (Fig. 10), owing to the different analysed subbases stiffnesses. The deflections calculated in the upper fibre of the CIR-base were reduced between 24% and 25% in the UGM_0 section, and between 15% and 16% in the UGM_H section. However, the differences between maximum and minimum deflections in the CIR-base in the sections with CTM subbase were always less than 6%. Thus, deflections and strains in sections with CTM not only presented a smaller variation, but even an opposite trend with the variation of the CIR-base thicknesses, as also occurred with the *SR*s (Fig. 10). As expected, deflections and strains estimated in the CIR-base were higher in the cases without HMA compared to those with HMA. And in the case with HMA, the deflections measured in the HMA and the CIR material (in the respective upper fibres) were practically the same, as is logical.

5.4. Influence of subbase type and CIR-base thickness on the rutting response

The results of the two sections cured (60 d) with HMA, using semi-rigid and flexible subbases, were used to analyse the response to rutting. A permanent deformation model with parameters previously fitted using actual results from repeated load triaxial tests was used (Table 2). The obtained *SR*s were introduced in expression (5), obtaining the predicted vertical strains ε_{vp} in the CIR-base against *N*, corresponding to the number of loads equivalent to a 130 kN single axle load on the lane (Fig. 13).

Permanent deformation limits of 2.00% and 4.00% were plotted in Fig. 13 to compare the different responses obtained. The standard EN 13286-7 [33] followed during the triaxial tests identifies the 2.00% of permanent deformation as an excessive level of deformations. However, other researchers consider 4.00% as a permanent deformation limit in BSM [12,19]. Similar to previous findings, when the subbase is flexible (UGM), increasing the thickness of the CIR-base led to improved overall behaviour of the section. In this case, it led to reaching the permanent

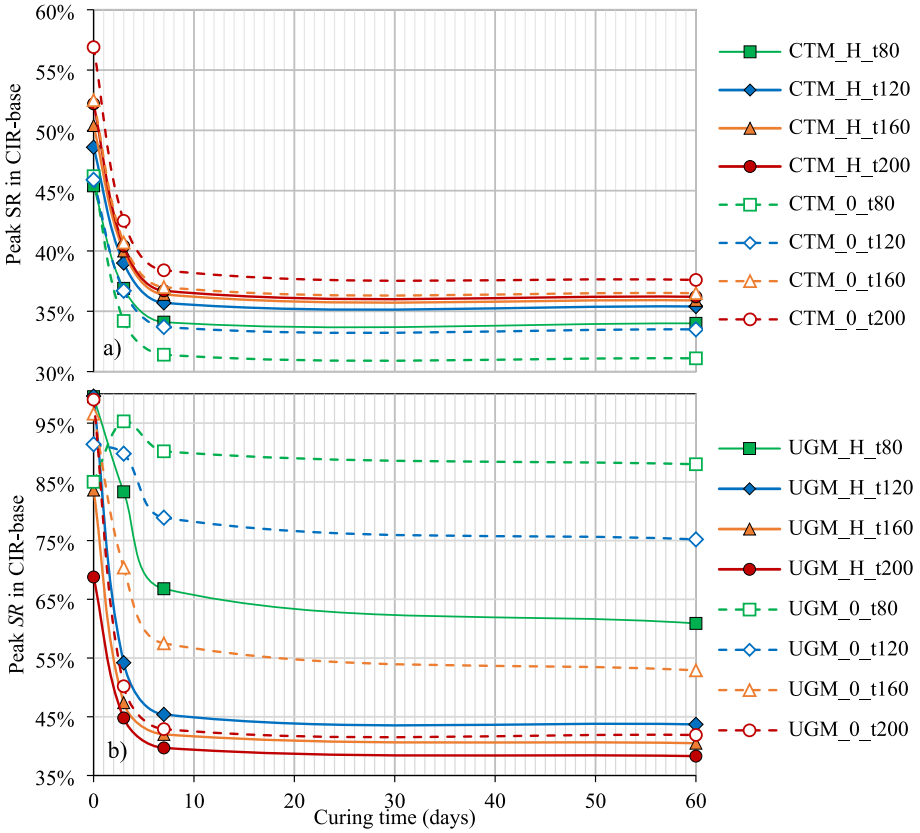

Fig. 11. Variation of the peak stress ratios with curing time: a) CTM subbase, b) UGM subbase.

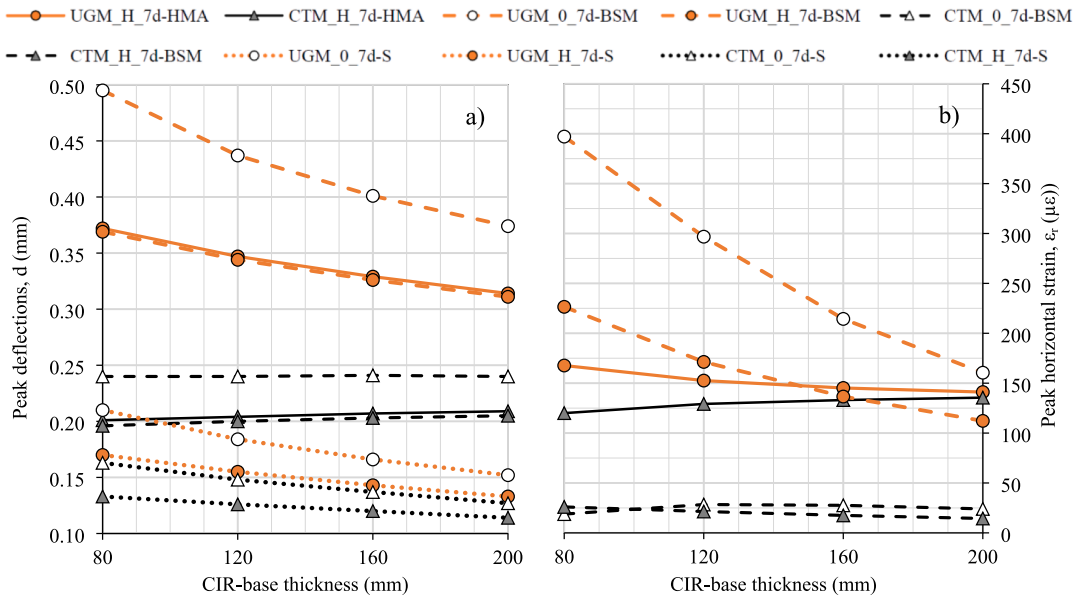

Fig. 12. Variation of the peak values of deflections and deformations according to the CIR-base thickness at 7 d of curing: a) Peak vertical deflections in the HMA, CIR material, and subgrade; b) peak horizontal strains in HMA and CIR material.

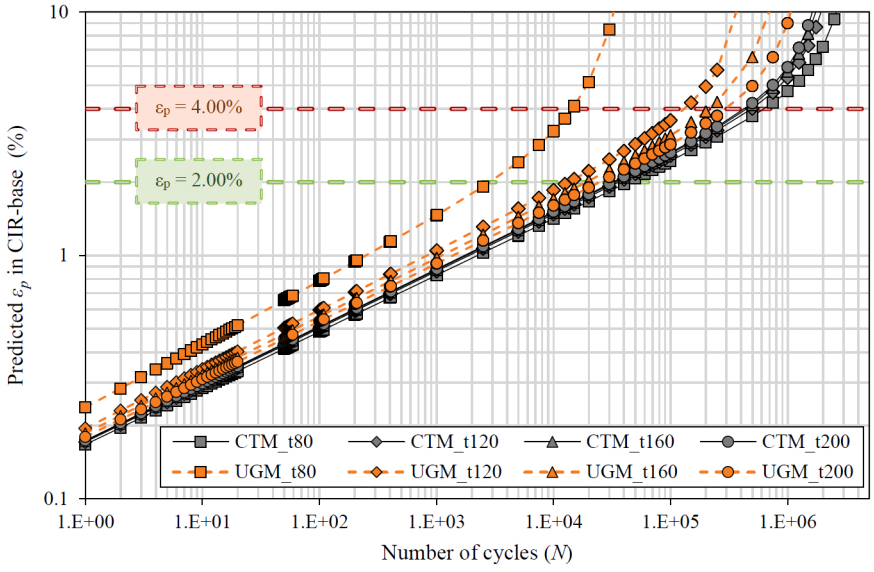

Fig. 13. Predicted vertical permanent strain in the CIR material base-layer for the two subbase types and four CIR-base thicknesses analysed.

deformation limits for a higher number of load cycles. However, the opposite occurred when the subbase was semi-rigid. Given that in CTM-subbase sections the CIR material is the weakest material, an increase in the CIR-base thickness led to earlier permanent deformations. Once again, the differences related to the CIR-base thickness are more significant for the UGM-subbase sections, while those with CTM-subbase showed less variation in terms of permanent deformation.

It was possible to transform the vertical deformations into rut depths by taking into account the base-layer thickness in each case. This estimated rut depth is the value corresponding to the permanent deformation of the CIR material of the base, and the different results allow to appreciate the influence of the studied variables. The total rut depth of the section will therefore be greater, caused by deformations not only at the base but in all layers (HMA, subbases, and subgrade). HMA and subgrade materials are the same in all the considered sections, however, it is important to note that sections with UGM subbase will present higher rut depths than those with CTM subbase. Fig. 14 shows these predicted rut depths in the CIR material base, for the two sections with HMA at 60 d of curing.

The Stellenbosch BSM Design described in TG2 specifies rutting limits between 10 mm and 25 mm depending on the road category, so horizontal lines indicating such rutting depth values have also been plotted in Fig. 14 as reference. When the subbase was CTM, rutting is expected to take longer to occur for the lowest CIR-base thicknesses, between 80 and 120 mm (values recommended by the Spanish PG-4). However, in the case of a UGM subbase, sections with greater CIR-base thickness showed earlier initial rutting but presented excessive values later than with smaller thicknesses. It should be noted that this result is in some sense expected because pavements with granular subbases are usually designed for lower traffic categories roads, and therefore for a lower number of design cycles. In contrast, pavements with cement-treated or cement-stabilized bases tend to be used for

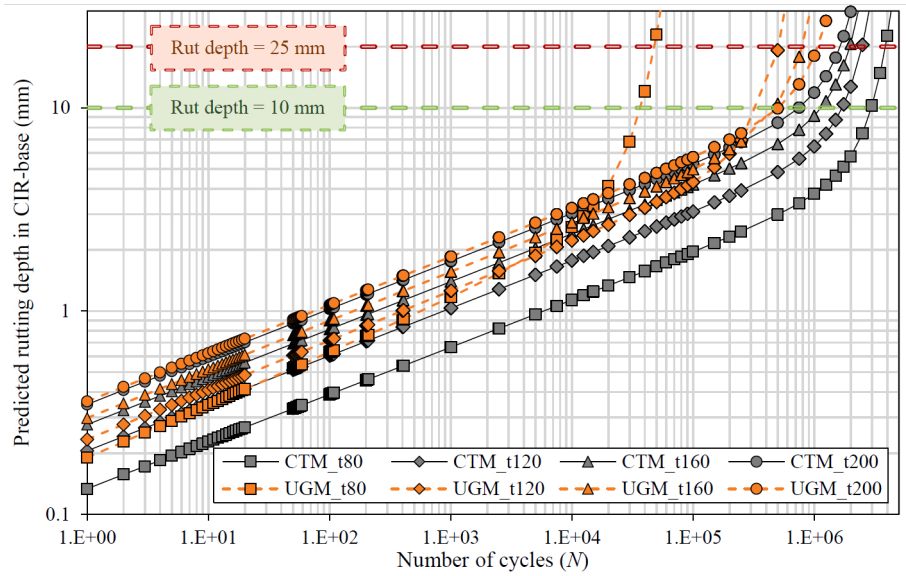

Fig. 14. Predicted rutting depth in the CIR material base-layer for the two subbase types and four CIR-base thicknesses analysed.

higher traffic categories, and therefore designed to withstand a greater number of cycles.

It is considered interesting for future research to include more accurate behavioral models for the rest of the materials included in the pavement section, in addition to the recycled material. For example, the use of stress-dependent models in the case of granular materials, consideration of temperature for viscoelastic materials, thus obtaining a more accurate prediction of the response of the complete pavement section.

6. Conclusions

In this study, the stress-dependent mechanical behaviour of the base-course in cold in-place recycling (CIR) rehabilitation was investigated. This behaviour was simulated with predictive models adjusted through triaxial tests results, which were carried out at different curing ages (0 d, 3 d, 7 d, and 60 d). The influence of curing time, base-course thickness (ranging from 80 to 200 mm), type of subbase (flexible or semi-rigid), and the effect of the wearing-course were analysed. The resulting stress ratios were used to feed a previously fitted permanent deformation model used to predict rutting occurrence and depth in each case. The following conclusions were drawn from the results of the study:

- The CIR material of the base exhibited typical nonlinear stress-dependent behaviour in all cases analysed. The predicted *Mr* decreased with depth, as did the stresses. The lack of HMA wearing-course and the flexible subbase resulted in a CIR-base with higher Mr variations. The inclusion of the HMA wearing-course and the semi-rigid subbase produced more stable Mr variations.
- Increasing the CIR-base thickness caused significant decreases in *SR*s and deflections in the sections with flexible subbase. However, when the subbase was semi-rigid, the variations were minimal and in the reverse sense, with slight increases in *SR*s and deflections.
- The evolution of CIR material properties measured in terms of *SR* reduction stabilized after 7 d of curing. The differences between the *SR* at 60 d compared to 7 d were not significant, and 7 d was considered to be sufficient curing time before placing the HMA wearing-course.
- The predicted permanent deformations for sections with flexible subbase were more sensitive to the variations in CIR-base thickness than with semi-rigid subbase. The scenarios with highest peaks of *SR* had the earliest predictions of elevated permanent deformations. The rut depths corresponding to the CIR-base layer were estimated from the permanent deformations in this layer. Sections with semi-rigid subbase showed predicted rut depths in the CIR-base proportional to its thickness. However, when the subbase was flexible, greater CIR-base thickness resulted in early initial small rutting in the CIR-base, but later arrival of excessive values.

It should be noted that only the nonlinear stress-dependent behaviour of the CIR material has been taken into account in the present investigation. Such behaviour is particularly noticeable in the initial curing phase, which is reminiscent of the behaviour of unbound granular materials. However, when curing is completed, the behaviour is intermediate between granular material and HMA. For future research, the possibility of taking into account other variables, such as temperature- and frequency-dependent behaviour, especially for more advanced curing cases, is encouraged. In addition, the implementation of more accurate behavioural models for the remaining materials would enable even more accurate predictions of the response of the entire pavement section.

Authors contributions

P. O., I. P., and A. R. P designed the laboratory study required for the characterization of the CIR material.

P. O. adjusted the predictive models and designed the simulation scenarios.

L.M. carried out the simulations.

P.O., J.F-R., and I.P analysed the results of the simulations.

Declaration of Competing Interest

The authors declare that they have no known competing financial interests or personal relationships that could have appeared to influence the work reported in this paper.

Acknowledgements

The authors would like to acknowledge funding for the project BIA2016-80317-R from the Spanish Ministry of Economy and Competitiveness (MINECO), with an associated pre-doctoral scholarship for the training of research workers (FPI) BES-2017-079633. An special acknowledgement to the Universidade da Coruña/ CISUG for funding

Elsevier's open access charge.

References

[1] F. Xiao, S. Yao, J. Wang, X. Li, S. Amirkhanian, A literature review on cold recycling technology of asphalt pavement, Constr. Build. Mater. 180 (2018) 579–604, https://doi.org/10.1016/j.conbuildmat.2018.06.006.

[2] Wirtgen GmbH, Wirtgen Cold Recycling Technology, Wirtgen Cold Recycl. Technol. (2012) 367.

[3] D. Offenbacker, A. Saidi, A. Ali, Y. Mehta, C.J. Decarlo, W. Lein, Economic and environmental cost analysis of cold in-place recycling, J. Mater. Civ. Eng. 33 (2021) 04020496, https://doi.org/10.1061/(asce)mt.1943-5533.0003610.

[4] A. Pakes, T. Edil, M. Sanger, R. Olley, T. Klink, Environmental benefits of cold-in-place recycling, Transp. Res. Rec. J Transp. Res. Board. 2672 (2018) 11–19, https://doi.org/10.1177/0361198118758691.

[5] S. Jain, B. Singh, Cold mix asphalt: an overview, J. Clean. Prod. 280 (2021), 124378, https://doi.org/10.1016/j.jclepro.2020.124378.

[6] G. Tebaldi, E. Dave, A. Cannone Falchetto, M. Hugener, D. Perraton, A. Grilli, D. Lo Presti, M. Pasetto, A. Loizos, K.J. Jenkins, A. Apeagyei, J. Grenfell, M. Bocci, Recommendation of RILEM TC237-SIB on cohesion test of recycled asphalt, Mater. Struct. 51 (2018) 117, https://doi.org/10.1617/s11527-018-1238-4.

[7] P. Orosa, A.R. Pasandín, I. Pérez, Assessment of two laboratory design methods for CIR mixtures with bitumen emulsion based on static and gyratory compaction, Constr. Build. Mater. 265 (2020), 120667, https://doi.org/10.1016/j.conbuildmat.2020.120667.

[8] G. Flores, J. Gallego, L. Miranda, J.R. Marcobal, Cold asphalt mix with emulsion and 100% rap: compaction energy and influence of emulsion and cement content, Constr. Build. Mater. 250 (2020), 118804, https://doi.org/10.1016/j.conbuildmat.2020.118804.

[9] P. Orosa, I. Pérez, A.R. Pasandín, Short-term resilient behaviour and its evolution with curing in cold in-place recycled asphalt mixtures, Constr. Build. Mater. 323 (2022), 126559, https://doi.org/10.1016/j.conbuildmat.2022.126559.

[10] E. Santagata, G. Chiappinelli, P.P. Riviera, O. Baglieri, Triaxial testing for the short term evaluation of cold-recycled bituminous mixtures, Road Mater. Pavement Des. 11 (2010) 123–147, https://doi.org/10.1080/14680629.2010.9690263.

[11] P. Orosa, I. Pérez, A.R. Pasandín, Evaluation of the shear and permanent deformation properties of cold in-place recycled mixtures with bitumen emulsion using triaxial tests, Constr. Build. Mater. 328 (2022), 127054, https://doi.org/10.1016/j.conbuildmat.2022.127054.

[12] K.J. Jenkins, F.M. Long, L.-J. Ebels, Foamed bitumen mixes = Shear performance? Int. J. Pavement Eng. 8 (2007) 85–98, https://doi.org/10.1080/10298430601149718.

[13] A. Saidi, A. Ali, Y. Mehta, B.C. Cox, W. Lein, Evaluation of Laboratory and Field Performance of Cold In-Place Recycling (CIR) Asphalt Mixtures, in: Proc. RILEM Int. Symp. Bitum. Mater., 2022: pp. 803–809. 10.1007/978-3-030-46455-4_102.

[14] A. Vaitkus, J. Gražulytė, A. Baltrušaitis, J. Židanavičiūtė, D. Čygas, Long-term performance of pavement structures with cold in-place recycled base course, Balt. J. Road Bridg. Eng. 16 (2021) 48–65, https://doi.org/10.7250/bjrbe.2021-16.523.

[15] A. Graziani, C. Iafelice, S. Raschia, D. Perraton, A. Carter, A procedure for characterizing the curing process of cold recycled bitumen emulsion mixtures, Constr. Build. Mater. 173 (2018) 754–762, https://doi.org/10.1016/j.conbuildmat.2018.04.091.

[16] S.M. Saeed, M.H. Sutanto, M. Napiah, F. Wong, M. Bujang, Review on the Effect of Curing on Cold Recycled Asphalt Mixture, in: 2021: pp. 1052–1060. 10.1007/978-981-33-6311-3_119.

[17] F. Lekarp, U. Isacsson, A. Dawson, State of the art. I: Resilient response of unbound aggregates, J. Transp. Eng. 126 (2000) 66–75, https://doi.org/10.1061/(ASCE)0733-947X(2000)126:1(66).

[18] W. Fedrigo, W.P. Núñez, M.A. Castañeda López, T.R. Kleinert, J.A.P. Ceratti, A study on the resilient modulus of cement-treated mixtures of RAP and aggregates using indirect tensile, triaxial and flexural tests, Constr. Build. Mater. 171 (2018) 161–169, https://doi.org/10.1016/j.conbuildmat.2018.03.119.

[19] L.-J. Ebels, Characterisation of Material Properties and Behaviour of Cold Bituminous Mixtures for Road Pavements, Stellenbosch University, 2008.

[20] K.J. Jenkins, D.C. Collings, Mix design of bitumen-stabilised materials – South Africa and abroad, Road Mater. Pavement Des. 18 (2017) 331–349, https://doi.org/10.1080/14680629.2016.1213511.

[21] B. Gómez-Meijide, I. Pérez, Nonlinear elastic behavior of bitumen emulsion-stabilized materials with C&D waste aggregates, Constr. Build. Mater. 98 (2015) 853–863. 10.1016/j.conbuildmat.2015.07.004.

[22] Y.H. Huang, Pavement Analysis Design, second ed., Pearson Prentice Hall, Upper Saddle River, NJ, USA, 2004., second ed., Upper Saddle River, NJ, USA, 1993.

[23] I. Pérez, L. Medina, M.A. Del Val, Nonlinear elasto-plastic performance prediction of materials stabilized with bitumen emulsion in rural road pavements, Adv. Eng. Softw. 91 (2016) 69–79, https://doi.org/10.1016/j.advengsoft.2015.10.009.

[24] I. Pérez, L. Medina, B. Gómez-Meijide, P.A. Costa, A.S. Cardoso, Numerical simulation of bitumen emulsion-stabilised base course mixtures with C&D waste aggregates considering nonlinear elastic behaviour, Constr. Build. Mater. 249 (2020), https://doi.org/10.1016/j.conbuildmat.2020.118696.

[25] Itasca Consulting Group Inc., FLAC3D (Fast Lagrangian Analysis of Continua in 3 Dimensions), Version 3.10, User's manual, (2006).

[26] Spanish Ministry of Development, PG-4. Recycling of bituminous pavements and roadways. Circular Order 40/2017, (2017).

[27] Asphalt Academy, Technical Guideline (TG2) : Bitumen Stabilised Materials Southern African Bitumen Association (Sabita), Pretoria, South Africa, 2020.

[28] AENOR (Spanish Association for Standardisation and Certification), UNE–EN 1097–6. Tests to determine the mechanical and physical properties of aggregates. Part 6: Determination of particle density and water absorption., In Spanish, Madrid, 2006.

[29] AENOR (Spanish Association for Standardisation and Certification), UNE–EN 12697–1 Bituminous mixtures. Test methods for hot mix asphalt. Soluble binder content., In Spanish, Madrid, 2013.

[30] AENOR (Spanish Association for Standardisation and Certification), UNE–EN 1426. Bitumen and bituminous binders. Determination of needle penetration., In Spanish, Madrid, 2015.

[31] AENOR (Spanish Association for Standardisation and Certification), UNE–EN 1426. Bitumen and bituminous binders. Determination of needle penetration., In Spanish, Madrid, 2015.

[32] AENOR (Spanish Association for Standardisation and Certification), UNE-EN 12697-31. Bituminous mixtures. Test methods for hot bituminous mixtures. Part 31: Specimen preparation by gyratory compactor, in Spanish, Madrid, 2008.

[33] AENOR (Spanish Association for Standardisation and Certification), UNE-EN 13286-7. Unbound and hydraulically bound mixtures - Part 7: Cyclic load triaxial test for unbound mixtures, In Spanish, Madrid, 2008.

[34] R.G. Hicks, Factors Influencing the Resilient Response of Granular Materials, University of California, Berkeley, 1970.

[35] J. Uzan, M.W. Witczak, T. Scullion, R.L. Lytton, Development and validation of realistic pavement response models, in: 7th Int. Conf. Asph. Pavements, Nottingham, UK, 1992.

[36] NCHRP (National Cooperative Highway Research Program), Guide for Mechanistic-Empirical Design of New and Rehabilitated Pavement Structures. Part 2. Design Inputs, Final Report NCHRP 1–37A, 2004.

[37] M. Huurman, Permanent deformation in concrete block pavement (PhD Thesis), Delft University of Technology, Netherlands, 1997.

[38] Trabajos Bituminosos (TRABIT), SUELOCEM. Suelo cemento in situ, In Spanish, Madrid, 2014.

[39] G.E. Halsted, D.R. Luhr, W.S. Adaska, Guide to Cement-Treated Base (CTB), 2006.

[40] S. Erlingsson, S. Rahman, F. Salour, Characteristic of unbound granular materials and subgrades based on multi stage RLT testing, Transp. Geotech. 13 (2017) 28–42, https://doi.org/10.1016/J.TRGEO.2017.08.009.

[41] L. Medina Rodríguez, M. Melis Maynar, I. Pérez Pérez, La deformabilidad de la explanada y el análisis de firmes 2ª Parte: Comprobación estructural de las secciones de la 6.1 y 6.2 I.C, (n.d.).

[42] M.R. Thompson, R.P. Elliott, ILLI-PAVE-based response algorithms for pavements, Transp. Res. Rec. 1043 (1985) 50–57.

[43] Spanish Ministry of Development, 6.1-IC: Pavement Sections, (2003).

[44] Technical Association for Bituminous Emulsions (ATEB), Cold Recycling with Bitumen Emulsion, (2014).